Planetary and Space Science 57 (2009) 1022–1031

Contents lists available at ScienceDirect

Planetary and Space Science

journal homepage: www.elsevier.com/locate/pss

Water ice clouds in the Martian atmosphere: Two Martian years of SPICAM nadir UV measurements

N. Mateshvili *, D. Fussen, F. Vanhellemont, C. Bingen, E. Dekemper, N. Loodts, C. Tetard

Belgian Institute for Space Aeronomy, Avenue Circulaire, 3, B-1180 Brussels, Belgium

ARTICLE INFO

Article history:
Received 15 April 2008
Received in revised form
8 September 2008
Accepted 13 October 2008
Available online 29 October 2008

Keywords:
Mars
Water ice
Clouds
MEX
SPICAM
Mars atmosphere

ABSTRACT

The SPICAM instrument onboard Mars Express has successfully performed two Martian years (MY 27 and MY28) of observations. Water ice cloud optical depths spatial and temporal distribution was retrieved from nadir measurements in the wavelength range 300–320 nm. During the northern spring the cloud hazes complex distribution was monitored. The clouds in the southern hemisphere formed a zonal belt in the latitude range 30–60°S. The edge of the retreating north polar hood merged with the northern tropical clouds in the range 250–350°E. The development of the aphelion cloud belt (ACB) started with the weak hazes formation (cloud optical thickness 0.1–0.3) in the equatorial region. At the end of the northern spring, the ACB cloud optical thickness reached already values of 0.3–1. The ACB decay in the end of the northern summer was accompanied with a presence of clouds in the north mid-latitudes. The expanded north polar hood merged with the north mid-latitude clouds in the eastern hemisphere. The interannual comparison indicates a decrease in cloud activity immediately after a strong dust storm in southern summer of MY28. The strong dust storms of the MY28 may also be a reason of the observed north polar hood edge shifting northward by 5°.

1. Introduction

The water ice clouds are closely related to the Martian atmospheric circulation and are important in understanding the Martian water cycle. The clouds also play an important role in the water vapor vertical distribution (e.g. Clancy et al., 1996) and in the removal of atmospheric dust particles. Chemical reactions occurring on ice cloud particles are significant in the composition and evolution of the Martian atmosphere (Lefevre et al., 2008).

The Martian water ice clouds have been actively investigated during many space missions in a wide range of wavelengths.

James et al. (1994) observed the Martian clouds using Hubble Space Telescope (HST) measurements in the visible and the UV ranges. Clancy et al. (1996) observed by HST the aphelion cloud belt (ACB) and supposed that it is caused by condensation of water vapor lifted by the ascending branch of Hadley circulation. Wolff et al. (1999) continued the observations of the seasonal and interannual ACB and made some estimates of cloud optical thicknesses in the UV. SPICAM (Spectroscopy for the Investigation of the Characteristics of the Atmosphere of Mars), onboard Mars Express (MEX) satellite, continued Martian cloud monitoring in the UV and optical thickness distribution maps for one Martian year were presented in (Mateshvili et al., 2007a) (hereafter Paper I). Starting from November 2007 Mars Color Imager (MARCI) based on Mars Reconnaissance Orbiter provides daily global images of Mars at 5 visible and 2 ultraviolet wavelengths (Malin et al., 2008).

The Martian cloud distribution was observed from daily global imaging in blue filter by Mars Orbital Camera (MOC) onboard Mars Global Surveyor. Wang and Ingersoll (2002); Benson et al. (2003, 2006) used MOC blue and red wide angle images to obtain cloud distribution and its seasonal behavior.

Thermal IR measurements of Mars clouds have been performed by many instruments. Tamppari et al. (2000) used Viking Infrared Thermal Mapper (IRTM) data to reconstruct the ice cloud distribution. Pearl et al. (2001); Smith et al. (2003a, b) and Smith (2004) retrieved ice cloud optical thicknesses and built a cloud distribution map from Thermal Emission Spectrometer (TES) infrared spectral observations. (Clancy et al., 2003) (companion paper with Wolff and Clancy, 2003) determined the distinct cloud particle sizes of the ACB from measured visible/IR opacity ratios, and defined two distinct cloud types based on particle size, scattering phase function, and distribution (type 2 particles in the ACB). Tamppari et al. (2008) used the TES data to investigate ice cloud distributions in the polar regions. Smith et al. (2003a, b) retrieved water ice cloud optical depths from Thermal Emission Imaging System (THEMIS) measurements and compared the results with TES measurements. TES and THEMIS data sets were acquired for different local times, providing constraints on the diurnal evolution process of clouds. Zasova et al. (2005) retrieved

* Corresponding author.
E-mail address: ninam@aeronomie.be (N. Mateshvili).

0032-0633/$ - see front matter © 2008 Elsevier Ltd. All rights reserved.
doi:10.1016/j.pss.2008.10.007

cloud optical thicknesses for several orbits from measurements of Planetary Fourier Spectrometer (PFS), an instrument onboard MEX.

In this paper, we present two Martian year measurements of water ice cloud optical thickness distribution by the SPICAM experiment. The paper is a continuation of the previous work (Paper I), where the results of one Martian year measurements were presented. The dataset covers more than two Martian years (Clancy et al., 2000): from 9 January 2004 (MY26, orbit 8, solar longitude $L_s = 331^\circ$), to 10 February 2008, (MY29, orbit 5278, $L_s = 30^\circ$).

2. The SPICAM instrument

SPICAM is a two-channel (UV and IR) slit spectrometer onboard Mars Express. Here we consider SPICAM UV channel nadir measurements. SPICAM employs a CCD array detector. Twenty CCD lines were used to register twenty spectra in each single measurement. The data were binned by four pixels in each CCD column due to telemetry restrictions and finally five spectra were transmitted every second, covering slightly different spatial areas. The measurements cover the wavelength range 118–320 nm but, due to strong CO_2 absorption at shorter wavelengths, only the 200–320 nm band is considered. The calibration was performed using SPICAM UV stellar measurements above the atmosphere (Bertaux et al., 2006). A detailed description of the instrument is given by Bertaux et al. (2000). The spectra present average spatial resolution of 1.2 km across the track and 2.4 km along the track (Perrier et al., 2006). The measurements were made every second.

3. Observations

Fig. 1 presents the orbital coverage for the considered SPICAM data set. The plain-parallel radiative transfer code used in this paper (see Section 4) gives correct results only for moderate solar zenith angles (SZA). Therefore only measurements with SZA less than 85° were included in Fig. 1. There are essential gaps in the measurements that in many cases complicate interannual comparison of the cloud optical thickness distributions.

The data quality is not uniform throughout the dataset. Starting from the orbit 2603, the data exhibit sporadic spikes (Fig. 2a). Sometimes the signal jumps down (Fig. 2b). Both sporadic spikes and signal jumps uniformly affect the whole spectrum. The origin of spikes and jumps may be connected with CCD high voltage power supply improper behavior. The signal, expressed in ADU (analog to digital units), was spectrally averaged (Fig. 2, dotted line). All data were browsed and all the spikes and jumps of signal were carefully excluded. The data quality flag files for every data point were created. The signal jumps were excluded manually, whereas for the spike removing a semi-automatic algorithm was developed. The spike detection algorithm was based on the well-known low-pass filter technique. As it is possible to see from Fig. 2 the quality of the spike removal is good. The consequence of the spike and jump presence is that the data have been partly lost and that the level of noise in the rest of data sometimes increased due to lower parts of spikes which have passed through the filter. The spike detection was made under a careful visual control. The signal can sharply vary not only due to spikes but also due to a sharp change of the surface altitude that causes a change of the air pressure and hence the intensity of Rayleigh scattering. The spectrally averaged signal was compared with the surface altitude of the observed area extracted from MOLA (Mars Orbiter Laser Altimeter) maps (Smith et al., 2003a, b). One more cause of the sharp signal change can be the presence of surface ices. The MOC maps were used to exclude the data points where the signal sharply increased due to an increase of the surface albedo. The developed algorithm works well with relatively smooth signal increases as in the case of clouds (Fig. 2a).

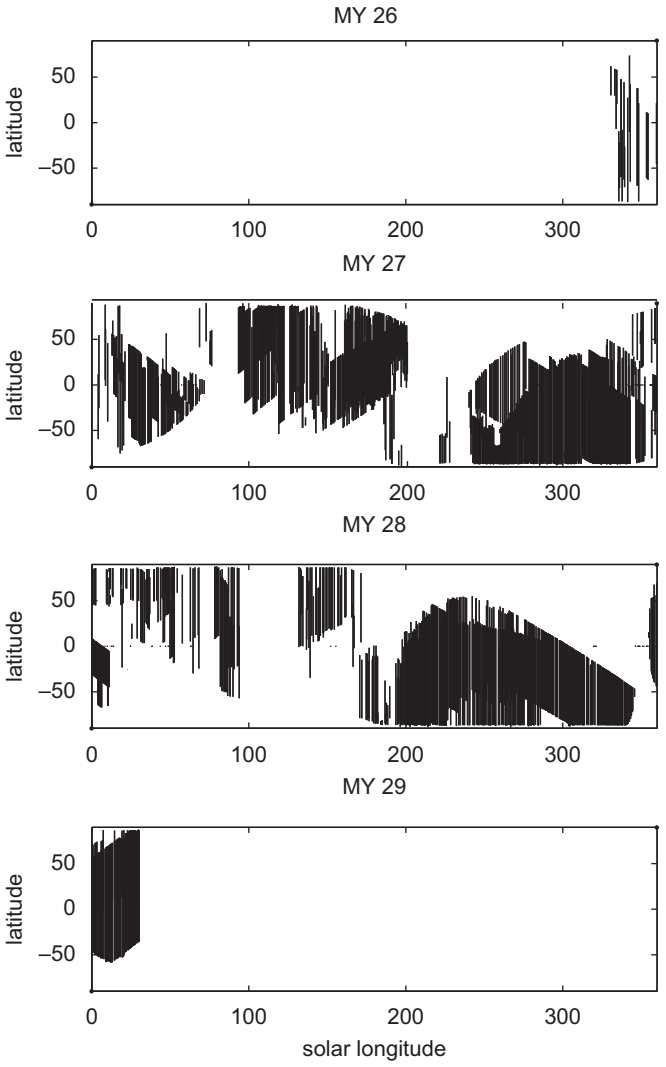

Fig. 1. Orbit distribution as a function of the latitude and the solar longitude. Only parts of orbits with $SZA < 85^\circ$ are presented.

4. Cloud optical thickness retrieval

The applied procedure for the cloud optical thickness retrieval was described in detail in Paper I. Here we only briefly repeat it.

The Martian surface albedo is low in the UV domain due to strong absorption by iron compounds which are abundant in the Martian soil (Bell, 1996). This gives an advantage of ice cloud retrieving. The bright clouds stand out in sharp contrast against the dark Martian soil background.

The signal in the considered wavelength domain (200–320 nm) is sensitive to a few factors. The albedo of the Martian surface exhibits modest regional variations as well as strong increases associated with surface ices. The Martian surface roughness is responsible for non-Lambertian behavior, such as a strong opposition effect (Hapke, 1986). The effect causes an increase of signal, mainly due to shortening of shadows, at small phase angles of measurements. A surface pressure variation is connected with the surface altitude variation of the sharp Martian relief that

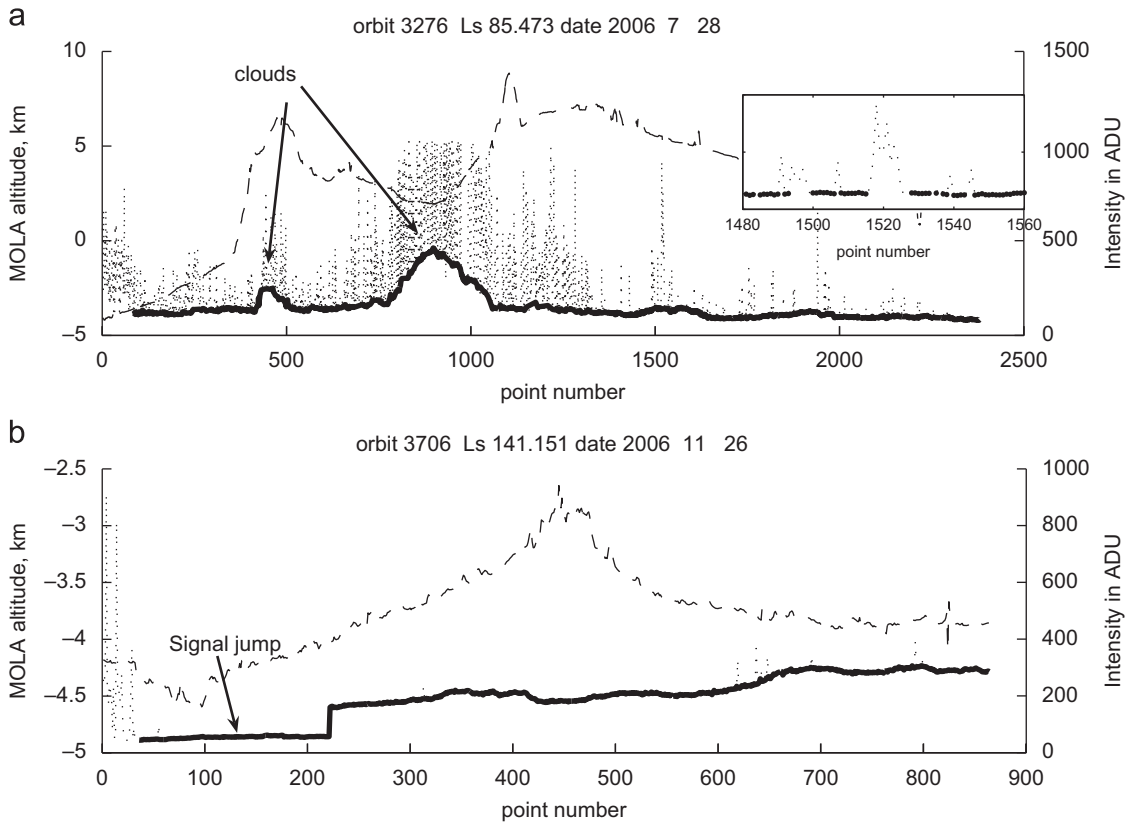

Fig. 2. Spectrally averaged intensity in ADU (analog to digital units) before (dotted line) and after (solid line) spike removal. The corresponding surface MOLA (Mars Orbiter Laser Altimeter) altitude is indicated by dashed line. (a) A typical example of cloud detection from orbit, contaminated by spikes. Inset shows spikes in detail. The orbit crosses Alba Patera and Tharsis region. (b) A typical example of signal jump. The orbit crosses Nili Fossae and Isidis Planitia.

modulates Rayleigh scattering, an important source of scatterng in the UV even for the thin Martian atmosphere. The surface pressure was extracted from the GCM calculations (Forget et al., 1999), and the pressure profile was calculated using the hydrostatic equation. There is a thin ozone layer in the Martian atmosphere. Ozone is abundant mainly in the polar regions during winter time. The ozone Hartley band is centered at 260 nm, that is, in the considered range of wavelength. The Martian dust single scattering albedo is low in the UV and increases with wavelength (Mateshvili et al., 2007b). The dust presence causes wavelength dependent signal decrease. Ice clouds also contribute some increases of the signal in the UV.

To reduce the number of retrieved parameters the following retrieval strategy was used. The signal was averaged through the narrow wavelength domain 300–320 nm (cited below as 'SPICAM red band'). This spectral range minimizes Hartley ozone band absorption, especially associated with the very low ozone columns (maximal observed value 33 μm-atm, Perrier et al., 2006) characteristic of the Mars atmosphere. Neglecting the effects of dust scattering/absorption is more problematic, as dust appears distinctly bright against the surface in MOC imaging (Cantor et al., 2001). However, Mateshvili et al. (2007b) showed that, contrary to its behavior in the visible range, Martian dust exhibits absorptive features in the UV and this absorptive effect increases with the decreasing wavelength. The absorptive effect of dust was very clearly observed during a few dust storms (Mateshvili et al., 2007b). The effect of dust presence appears to be minimal at about 300 nm wavelength. Around this wavelength the effect of dust can be considered as incorporated in the retrieved 'apparent' surface albedo values.

The cloud retrieval was performed in two-steps procedure (Paper I). First, the 'apparent' albedo values were retrieved from the SPICAM red band values (S_r). The observed variations of S_r were fitted by a radiative transfer code using only one fitting parameter—a Lambertian surface albedo. Water clouds manifested themselves as an increase of the 'apparent' albedo values. The 'apparent' albedo database was browsed and a cloud detection threshold albedo value was derived by comparison of "apparent albedos" for orbits with and without clouds, where clouds were detected from raw data (see Paper I for details). The apparent albedo threshold value was estimated as 0.02. The 'apparent' albedo values were sorted with respect to the threshold. Orbit segments with and without clouds were separated. Regions covered with surface ices were excluded using MOC (Benson and James, 2005) and TES (Christensen et al., 2001; Titus, 2005) data. The orbit segments without clouds were corrected for the opposition effect (Paper I). Then a Martian surface albedo map was created. For this purpose, we had to use not only orbits attributed to the dry perihelion season but also orbit segments without clouds acquired during wet aphelion season due to insufficient orbital coverage and strong dust storms observed in the second part of the MY28. The surface of Mars was divided in 4.5° bins and for each bin the most probable apparent albedo value was sought. This procedure emphasizes low aerosol haze conditions to derive a surface albedo map, although a bias remains due to some minimal amount of dust which is always present in the Martian atmosphere. The surface albedo map was used on the second retrieval step, when clouds were retrieved from orbit segments for which the apparent albedo values were above the threshold. Only clouds with optical depth higher then 0.05 (which roughly corresponds to 10% of apparent albedo variation) were included in the cloud database. The uncertainties of the retrieval procedure were analyzed in Paper I and here we only give a summary.

The plane-parallel multiscattering radiative transfer code SHDOM (Evans, 1998) was used for the modeling. The water ice cloud optical properties were described using the Henyey—Greenstein phase function with the asymmetry parameter $g=0.7$ and the single scattering albedo $w=1$ (see Paper I for the water ice cloud optical properties discussion). The water ice cloud asymmetry factor g is not known well in the UV. The adopted value of g is a compromise between different estimates. Clancy and Lee (1991) obtained a value $g=0.66$ using emission phase function measurements by the Viking IRTM broadband (0.3–3.0 μm) visible channel centered at 0.67 μm. Key et al. (2002) modeled properties of the Earth's cirrus clouds and obtained $g=0.75$ for solid columns of effective radius 6 μm at 300 nm wavelength. Clancy et al. (2003) identified two types of Martian ice clouds with particle effective radius 1–2 μm and 3–4 μm analyzing TES emission phase function observations. They also estimated $g=0.62$–0.63, and 0.66–0.68 for both ice cloud types by fitting emission phase function forward peaks. We cannot directly employ the emission phase functions derived in Clancy et al. (2003) due to the significant difference in the wavelength of measurements (0.3 μm in this work and TES solar band channel 0.4–2.8 μm, centered at 0.7 μm). We estimated the value of g for particle effective radii 2 and 4 μm using the Mie theory and water ice optical properties at 0.67 μm (Warren, 1984). The result was ~0.85 for both particle effective radii 2 and 4 μm. This value differs significantly from Clancy and Lee (1991) and Clancy et al. (2003) results. This discrepancy forced us to adopt a compromise value $g=0.7$. In Paper I, we discussed a possibility to rescale optical depths to a different value of g. Keeping in mind such a possibility, we do not make any difference between the two types of ice clouds in the retrieval procedure.

The cloud top altitudes were assumed 25 and 20 km for the ACB and the polar hoods correspondingly, with 10 km thickness. The error analysis (Paper I) has shown that the retrieved optical thicknesses are only slightly influenced by an assumed cloud altitude if dust is not introduced in the model. It was estimated (Paper I) that both dust and surface albedo errors cause the following uncertainties: 40% for SZA$<30^\circ$, 20–30% for SZA $>30^\circ$ and up to 50% for SZA $>75^\circ$. The asymmetry factor error $g=0.7\pm0.05$ gives 17% uncertainty.

5. Cloud distribution

In this section, ice cloud optical depth seasonal distribution and some interannual variations will be discussed. Due to highly elliptical orbit, Martian weather exhibits essential differences between cold and cloudy aphelion season ($L_s=0$–180°) and relatively hot perihelion dust storm season ($L_s=180$–360°) (Clancy et al., 1996). Below we consider the evolution of major Martian cloud structures such as north and south polar hoods and ACB during more than two Martian years. Whereas a lot of Martian toponyms are cited in this paper, we refer to a map of Mars (http://ralphaeschliman.com/mars/mltsm.pdf, western longitudes are used). Before starting a detailed description of ice cloud distribution we should say a few words about dust storms that occurred during the period of measurements. The period covers two dust storm seasons, in MY 27 and 28, and the end of the dust storm season of MY26. TES measurements (e.g. Lewis et al., 2006) registered a dust storm in the range $L_s=315$–335° in MY26. They estimated equivalent optical depth at 6 mbar as 1–2. SPICAM measurements give very close values for the same period (unpublished data). MY 27 dust storm season also was relatively calm. A series of regional dust storms were observed by HST (http://hubblesite.org/newscenter/archive/releases/2005/34/image/a) and ground based telescopes (McKim, 2006) in October, 2005 ($L_s=312^\circ$) over Chryse Planitia (20°N, 315°E) and then southward. One episode of the dust storm was analyzed in Mateshvili et al. (2007b). The dust cloud optical thickness was estimated as 2.5. Dust storms in July 2007 (MY28) were significantly more intensive and wide-spread. Mars Exploration rover Opportunity registered dust optical thickness up to 5 (http://marsrovers.jpl.nasa.gov/gallery/press/opportunity/20070720a.html). The same dust optical thickness value was observed by SPICAM (Mateshvili et al., 2007b) during the MY28 dust storm in the $L_s=270$–310° period (Mateshvili et al., 2007b).

5.1. Seasonal behavior

In this section, water ice cloud seasonal distribution is presented (Fig. 3). The whole dataset from the end of MY26 to the beginning of MY29 was considered. The measurements acquired in MY28 and the beginning of MY29 mainly are complementary to the MY 27 and the end of MY26 measurements (Fig. 1). All cases of measurement overlapping are considered to study interannual variabilities (Section 5.3).

Fig. 3 shows the zonal means of cloud optical thicknesses based on the whole dataset as a function of the solar longitude (L_s). The similar map for the MY27 was presented in Paper I. The data were averaged over 1° of latitude and 1° of L_s. Grey background on Fig. 3 shows orbit distribution. It was not possible to distinguish between surface ices and clouds, therefore the area covered by polar ices was excluded from the ice cloud distribution map. This is the reason why on Fig. 3 there are no clouds in polar regions.

An important parameter for a correct comparison of different ice cloud datasets is the local time (Fig. 4), because ice cloud optical thicknesses exhibit essential diurnal variation with the tendency to grow in the afternoon (Wolff et al., 1999; Smith et al., 2003a, b).

The general structure of the Martian cloudiness (Fig. 3) resembles very much that obtained by Smith (2004) from TES measurements. Many of features described below were observed also by Wang and Ingersoll (2002) and Tamppari et al. (2000).

In the first part of the wet and cool northern spring ($L_s=0$–60°), cloud hazes were observed almost at all latitudes. In the northern high latitudes the edge of the retreating north polar hood was registered above 40–60°N. It is difficult to distinguish between the edge of the north polar hood and mid-latitude clouds from Fig. 3, because they merge above Tempe Terra (40°N, 300°E). The border between these two groups of clouds is more distinct on Fig. 5, where the cloud optical depths are presented as a function of latitude and longitude for the considered L_s period. In the southern hemisphere cloud hazes were detected between 30°S and 70°S. And in the equatorial region the hazes partly covered the latitude belt 20°S–20°N.

The north polar hood disappeared with the progress of the northern summer (Fig. 3, $L_s=90$–140°) giving place to detached north polar summer clouds. After $L_s=140^\circ$ the northern high latitude cloudiness progressed and at $L_s=160^\circ$ the north polar hood was again visible. The south polar hood was mainly out of the zone of observations and only its edge was registered between $L_s=140^\circ$ and 200°. The most striking cloud structure during the northern summer was the ACB which developed near the equator, at $L_s\sim80^\circ$ in the low northern latitudes. Weak equatorial hazes transformed into well-developed clouds at the end of the northern spring. The ACB existed till the middle of the northern summer (at $L_s\sim140^\circ$) and then quickly dissipated. Weak hazes in the equatorial region still existed till the middle of the southern spring. During the southern winter and the southern spring the edge of the south polar hood was occasionally observed. During

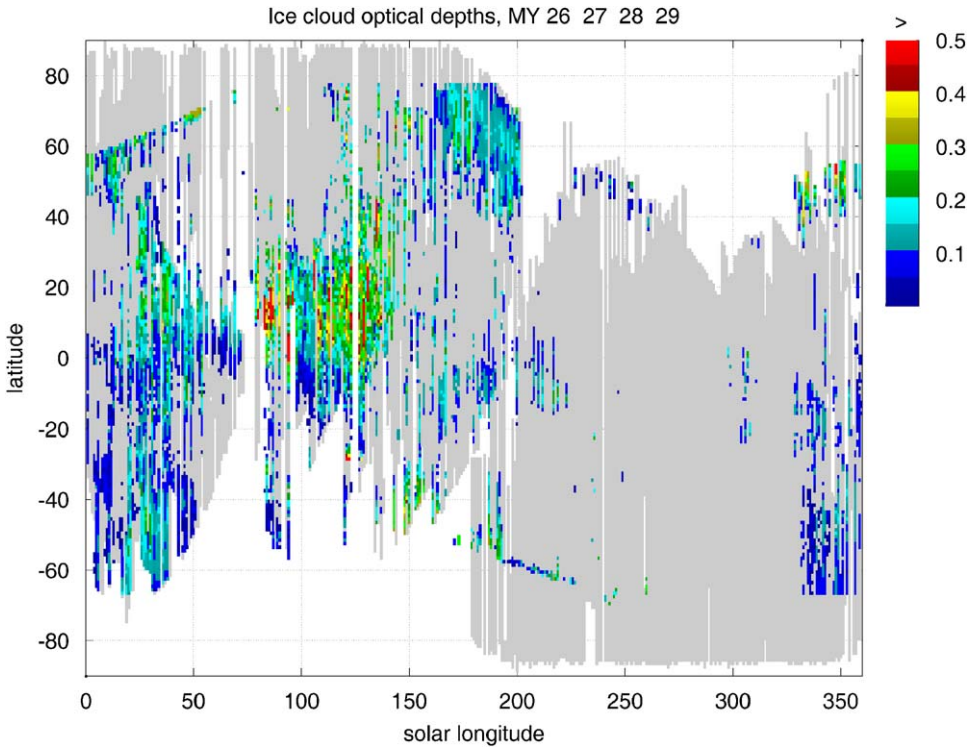

Fig. 3. Zonally averaged cloud optical depths vs. L_s based on the whole dataset. Grey background shows orbit distribution.

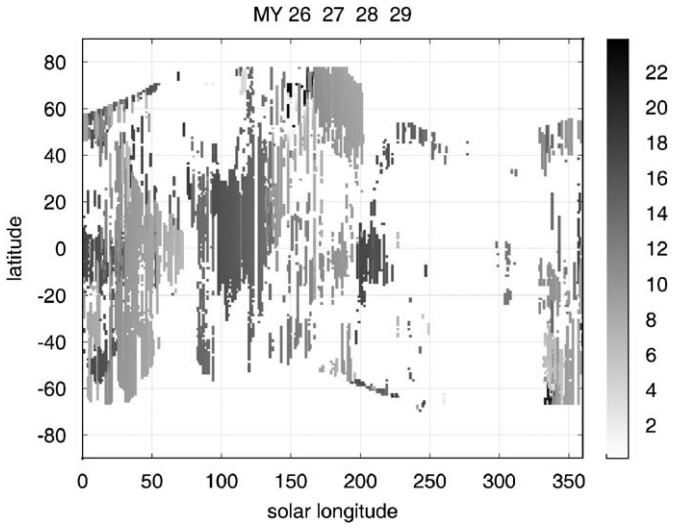

Fig. 4. Local time distribution for the cloud dataset presented on Fig. 3.

the southern summer ($L_s = 180–270^\circ$), the main cloud structure in the Martian atmosphere is the north polar hood (e.g. Wang and Ingersoll, 2002). The orbit distribution allowed to observe it only partly in the solar longitude range $L_s = 180–200^\circ$ in MY27 and in the range $L_s = 220–260^\circ$ in MY28.

In the southern fall, after the end of the summer dust storms, ice hazes appeared again in the equatorial region and in the southern mid-latitudes ($L_s = 330–360^\circ$). The edge of the retreating north polar hood was detected between 38° and 45° N.

5.2. *The MY28—Beginning of MY29 measurements*

The second (MY28) and the beginning of the third (MY29) Martian years of SPICAM measurements cover some important periods of cloud formation (Figs. 1 and 3). In MY28, SPICAM observed the development ($L_s = 68–95^\circ$) and decay ($L_s = 140–150^\circ$) stages of the ACB (Figs. 1 and 3). These two time intervals fill the gaps in the MY27 ACB observations. The last clouds in the equatorial region before the start of the dust storms were observed during the beginning of the southern spring ($L_s = 195–225^\circ$, Fig. 3). Hereafter the periods when the new measurements make contribution to the Paper I results are considered.

A complex structure of the ice hazes (MY27, 28, 29) was observed during the northern spring ($L_s = 0–60^\circ$, Fig. 5). The clouds in the southern hemisphere formed a zonal belt in the latitude range 30–60°S. As SPICAM orbits did not pass far southward in the considered period (Fig. 5), it is not possible to say if the observed zonal belt is separated from the south polar hood or is a part of it. Tamppari et al. (2000) reported about the mid-latitude belt prior to $L_s = 30^\circ$. Wang and Ingersoll (2002) observed south polar cap and hood growing northward from 60°S to 45°S during $L_s = 21–111^\circ$. Smith (2004) has also reported about clouds between 30°S and 60°S in the period $L_s = 0–50^\circ$. The clouds exhibited essential annual variation (Smith, 2004).

In the northern hemisphere the edge of the north polar hood was detected in 40–60°N range. The north polar hood merged with the northern tropical clouds above Tempe Terra (40°N, 300°E) and Acidalia Planitia (40°N, 330°E) in the range 250–350°E. The result is confirmed by MOC measurements (see Fig. 31 in Paper I or MOC image R1700547, http://www.msss.com/moc_gallery/). The fusion between the north polar hood and the northern tropical clouds was observed by TES (Smith, 2004). It is worth to mention that Fig. 5 combines three years of measurements. This fact complicates the data interpretation, but the result is confirmed by other instruments.

There were two centers of significant cloudiness in the equatorial region (Fig. 5). Clouds above Lunae Planum (20°N, 300°E) started to develop in early spring. Clouds above the second one, Syrtis Major (10°N, 70°E), developed later, at $L_s = 30–60^\circ$.

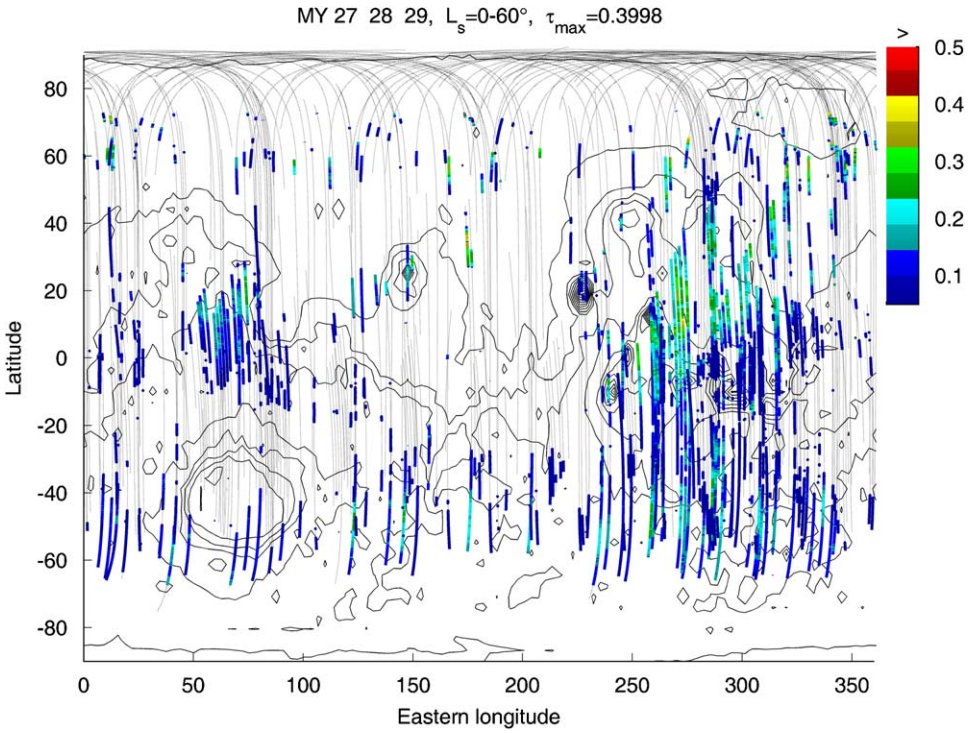

Fig. 5. Cloudiness for $L_s = 0$–60° superimposed on MOLA altitude map. Grey lines represent orbit tracks.

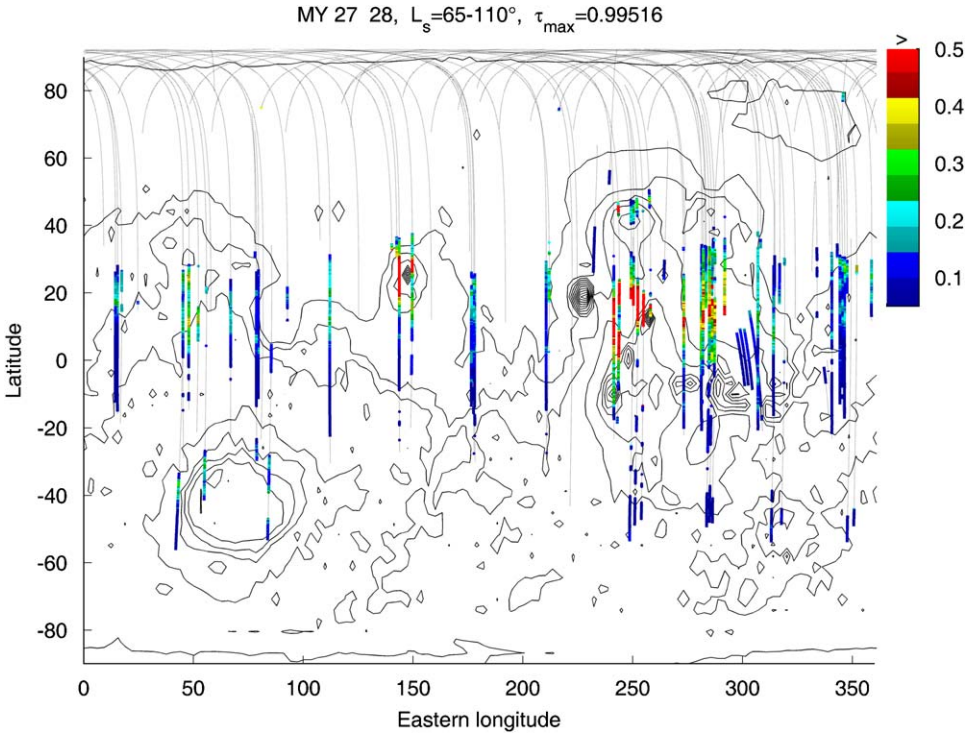

Fig. 6. The same as Fig. 5 for $L_s = 65$–110°.

Similar behavior was observed by Tamppari et al. (2000), whereas Wang and Ingersoll (2002) observed equatorial clouds growing at $L_s = 30$–60° not only above Syrtis Major but also in the large longitudinal sector 150–330°E.

Fig. 6 shows cloud distribution during the end of northern spring and the beginning of northern summer ($L_s = 65$–110°) observed in the MY27 and MY28. Fig. 6 shows further growth of cloudiness above Lunae Planum (20°N, 300°E) in comparison with Fig. 5. Besides of many orographic clouds above Tharsis region (10°N, 240°E), Alba Patera (40°N, 250°E) and Elysium Mons (25°N, 150°E) there were clouds above Arabia Terra (15°N, 30°E), Syrtis Major (10°N, 70°E), Elysium Planitia (10°N, 130°E) and Amasonis Planitia (30°N, 200°E), Lunae Planum and Chryse Planitia (25°N, 310°E). The presence of clouds, although not always very dense,

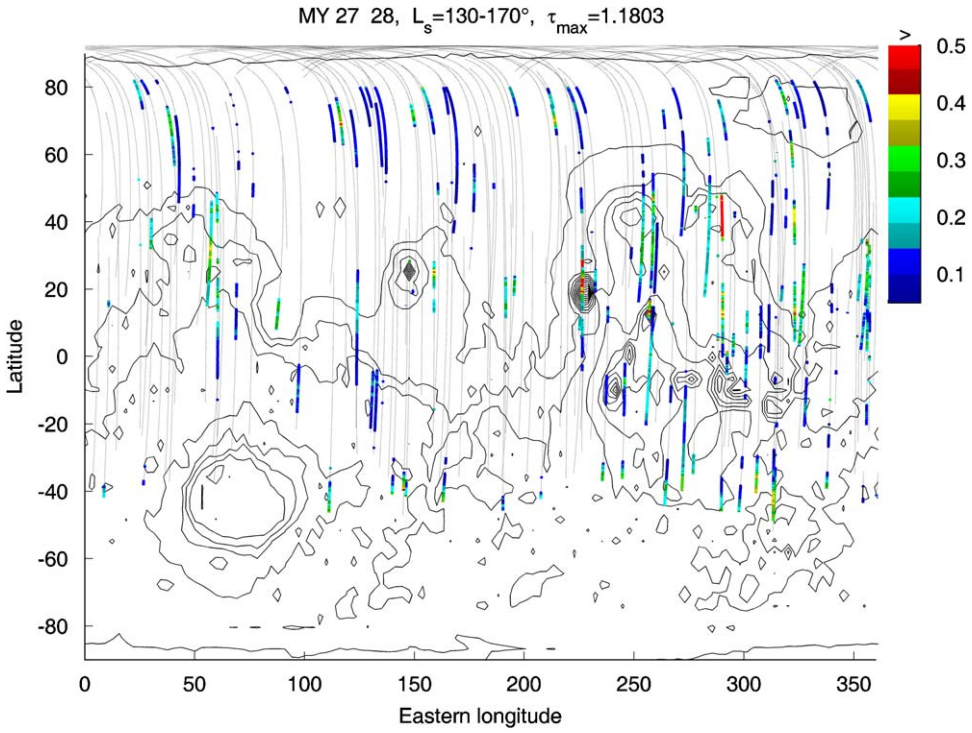

Fig. 7. The same as Fig. 5 for $L_s = 130–170^\circ$.

was observed almost everywhere in a zonal belt centered at 15°N and allows us to conclude that Fig. 6 presents the beginning stage of the ACB formation. Wang and Ingersoll (2002) observed the same cloud distribution between $L_s = 44^\circ$ and 70°. The same cloud structure was reported by Tamppari et al. (2000) at $L_s = 65^\circ$. All clouds on Fig. 6 are located southward of the latitude 40°N except for clouds above Alba Patera (40°N, 250°E). The presence of clouds above Alba Patera in the beginning of the ACB formation and during the decay of the ACB was mentioned by Benson et al. (2003). The maximum cloud optical thickness τ was higher in MY28 ($\tau_{max} \approx 1$) than in MY27 ($\tau_{max} \approx 0.7$).

Since there are only a few estimates of ice cloud optical depths in the UV, here we cite them to compare with our results. (Malin et al., 2008) estimated cloud optical depth at 0.5 above Hellas Planitia (40°S, 60°E) at $L_s = 132^\circ$, MY28 using the MARCI 320 nm band. SPICAM has measured the value 0.6 at $L_s = 122^\circ$, MY27 above almost the same place. Wolff et al. (1999) observed clouds with optical depth 0.1–0.3 at the wavelength 410 nm above Syrtis Major, Amasonis Planitia and Cryse Planitia during the northern summer. SPICAM results were 0.1–0.35.

The decay stage of the ACB in the second part of the southern summer is presented on Fig. 7 (MY27 and 28, $L_s = 130–170^\circ$). The ACB was still visible but became narrow in the longitudinal sector 0–200°E. Cloud activity was more intensive in the sector 220–360°E, where clouds there observed almost at all latitudes, starting from the edge of the retreating south polar hood at 40°S to the edge of the growing north polar hood at about 60°N. Through the period $L_s = 130–170^\circ$ the north polar hood grew, whereas equatorial clouds become more thin. TES (Smith, 2004) also observed a fusion between equatorial clouds and both north and south polar hoods in this period. The intensity of this phenomenon varied from year-to-year. MOC observations (Wang and Ingersoll, 2002) show equatorial clouds more separated from the both polar hoods. SPICAM cloud optical depth varied between 0.1 and 0.3 although separate clouds where significantly denser (1.1–1.2).

The last equatorial clouds observed in the beginning of the southern spring (Fig. 8a, MY27 and 28, $L_s = 200–250^\circ$) were those above Arsia Mons (10°S, 240°E). Benson et al. (2006, 2003) analyzed the seasonal behavior of clouds above the major volcanoes from MOC images. They received almost constant cloud activity above Arsia Mons with a gap at $L_s = 220–260^\circ$. Only a few thin clouds marked the edge of the north polar hood (MY28 data). It appeared about 5° northward from its location observed at $L_s = 200^\circ$ in MY27. There were higher dust loading in the period $L_s = 220–260^\circ$ of the MY28 than for $L_s = 200^\circ$ in MY27 (e.g. Mateshvili et al., 2007c). High dust loading of the atmosphere causes increase of the atmospheric temperature due to dust heating, which may account for the northward shift of the polar hood boundary in the MY28.

Measurements acquired during MY 26,27,28 contributed to the Fig. 8b ($L_s = 340–360^\circ$). The edge of the retreating northern polar hood was observed at 38–45°N. This is close to results of Smith (2004). The first clouds were registered in the southern hemisphere after dust storms during the southern summer. The clouds were significantly weaker in MY28 than MY27 clouds observed in the same season, perhaps due to a rise in atmospheric temperatures after the strong dust storms of MY28. Thin hazes in equatorial region also started to appear.

5.3. Interannual comparison of cloud optical depths

Below we compare the MY26, 27, 28 and 29 measurements. A map of coincidence was built (Fig. 9), where both temporal and spatial coincidences of cloud appearance in different years were considered. For this purpose a Martian year was divided in 36 time bins. The Martian surface was divided in 1° latitudinal and 10° longitudinal bins. The value of a bin was set to 1 when clouds attributed to different Martian years were noticed, otherwise the value of a bin was set to 0. Fig. 9 presents normalized zonal means of the bins. According to Fig. 9 the acquired data allow to make

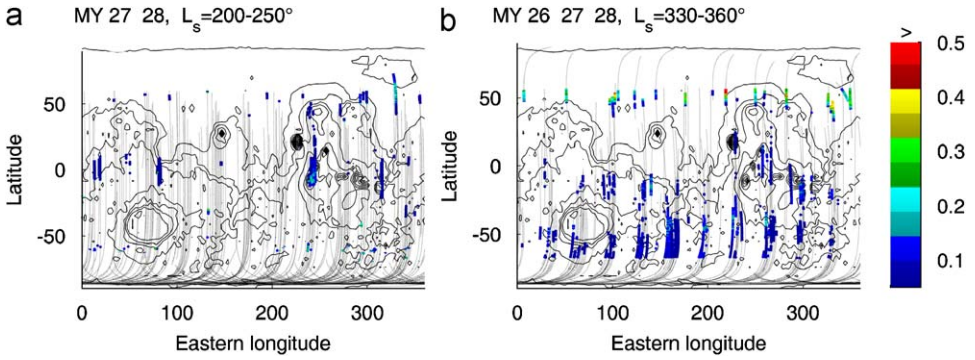

Fig. 8. (a) The same as Fig. 5 $L_s = 200–250^\circ$ and (b) the same as Fig. 5 for $L_s = 330–360^\circ$.

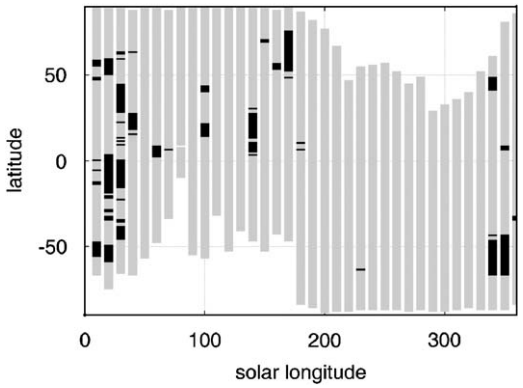

Fig. 9. A map of temporal and spatial coincidence of cloud appearance in different years (see text for details).

cloud optical depth interannual comparison for the following time ranges: the beginning of northern spring ($L_s = 0–40^\circ$), the middle of northern summer ($L_s = 130–140^\circ$), the end of northern summer ($L_s = 160–170^\circ$), the end of northern winter ($L_s = 330–360^\circ$).

When comparing optical depths of clouds observed in different Martian years we should take into account that the time of measurements varied from year-to-year. Smith et al. (2003a, b) had shown analyzing TES and THEMIS measurements that the ACB clouds grow in the late afternoon. Hinson and Wilson (2004) modeled night and daytime cloud distribution. They obtained that clouds should be more frequent in nighttime and diminish significantly during a day. That means there may be two types of variations superimposed in our data—interannual and diurnal.

Fig. 10 presents cloud optical depths observed in different Martian years for the solar longitude ranges cited above. In the beginning of northern spring (Fig. 10a), measurements acquired during three Martian years show good repeatability of the cloud optical depths although clouds observed in MY29 are slightly thinner. It is difficult to judge if it is still a consequence of the MY28 strong dust storm or some artifact.

Fig. 10b shows ACB cloud optical depth variations measured in the middle of northern summer. Both MY27 and 28 shows the presence of ACB clouds with the optical depth varying from 0.1 to 0.5, but MY27 data include some very bright clouds with optical depth up to 1. This rather reflects a variety of cloud brightness characteristic for that period as it is possible to see from Fig. 7.

Fig. 10c presents northern high latitude clouds in the end of northern summer ($L_s = 160–170^\circ$). MY28 measurements were acquired in the early morning and in the evening (SZA about 70°) whereas MY27 measurements were made in the late morning. The optical depth values are very similar for the both years.

In the end of the northern winter (Fig. 10d) clouds were observed during three Martian years: MY26, 27 and 28. These are the first clouds that reappeared after the dust storm season. Strong storms occurred just before the considered period of cloud formation in each of the three Martian years (see above the detailed description of the storms). Clouds observed in MY 28 were significantly thinner than in MY26 and 27. The reason of this difference may be connected with significantly higher intensity of the MY28 dust storm than the dust storms of MY26 and 27. The effect is possibly related to higher temperatures just after the strong dust storm of MY28. Benson et al. (2006) investigated the effect of the global 2001 dust storm (MY25) on cloud appearance above the major volcanoes using MOC images. The clouds above Arsia Mons typical for the period of observations disappeared totally during the dust storm and reappeared later and smaller in size.

6. Summary

In this paper, we present the Martian water ice cloud optical depth distribution obtained from nadir measurements of the SPICAM UV spectrometer onboard Mars Express satellite. The measurements cover the period of more than two Martian years from the end of the MY26 (January 2004, $L_s = 331^\circ$) to the beginning of MY29 (February 2008, $L_s = 30^\circ$). This paper is a continuation of work started in Paper I, where the results of MY 26 and 27 measurements were presented. Here we consider measurements acquired in MY28 and 29, combine the results with these of the previous year to fill the gaps in the cloud optical thickness distribution (Fig. 3) and make interannual comparison.

The Martian ice clouds manifest themselves as an increase of the measured UV brightness. The Martian soil has very low UV albedo that helps in cloud detection. The clouds were retrieved in a two step procedure. First, 'apparent albedo' values were retrieved from the signal averaged in wavelength domain 300–320 nm. The threshold value was introduced to separate orbit segments with and without clouds. The segments without clouds were used to build a ground albedo map (Paper I). Ice cloud optical depths were retrieved based upon the obtained albedo map for the segments where the apparent albedo value was higher than the threshold value.

The measurements acquired in MY 28 and the contribution of the beginning of MY29 increased the geographical, seasonal and interannual coverage of cloud optical depth distribution obtained from MY27 and the end of MY26 data (Fig. 3).

The MY28 and 29 data improve the definition of the cloud optical thickness distribution during the northern spring and southern summer (Fig. 5). Two distinct centers of cloudiness Syrtis Major (10°N, 70°E) and Lunae Planum (20°N, 300°E) were

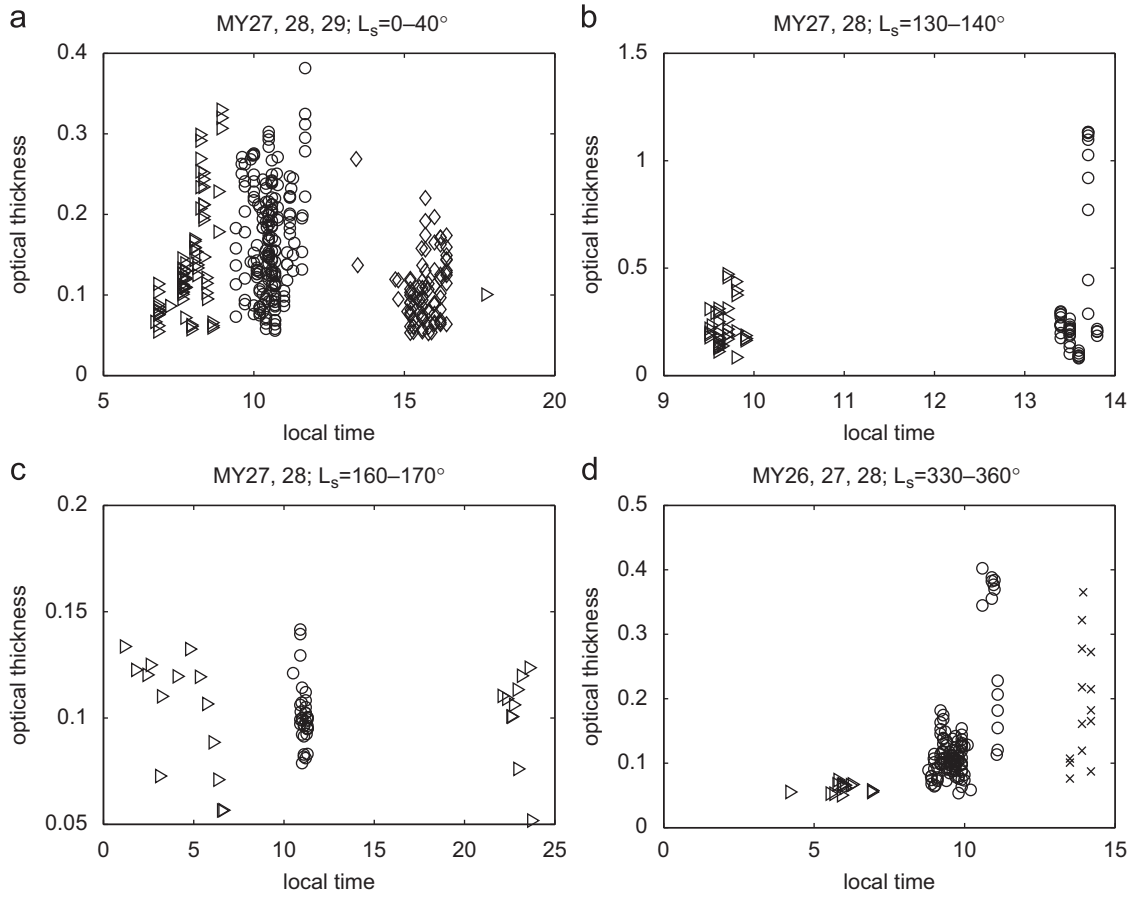

Fig. 10. Ice cloud depths observed in different years above the same places and in the same period of season. Crosses—MY26, circles—MY27, triangles—MY28 and diamonds—MY29.

detected in low latitudes. The zonal mid-latitude belt was observed in the southern hemisphere between 60°S and 40°S. It merged with the low latitude clouds in the sector 240–330°E. The presence of mid-latitude clouds in almost the same sector connected the low latitude clouds with the retreating north polar.

The ACB development and decay stages (Figs. 6 and 7) were monitored. Cloud activity was registered not only near the equator and in polar hoods but also in mid-latitudes. At the development stage (Fig. 6) only mid-latitude clouds where observed above Alba Patera (40°N, 250E°). This correlates with the results obtained by Benson et al. (2003, 2006), who registered two peaks of cloud activity above Alba Patera at $L_s = 60^\circ$ and 140°. At the decay stage (Fig. 7) mid-latitude clouds were observed in the sector 220–360°E. Smith, (2004) reported about the mid-latitude clouds in the same periods.

The interannual comparison (Figs. 9 and 10) revealed that clouds detected during the southern summer MY28 after a series of major dust storms appear to be less optically thick than for corresponding observations in MY26 and 27 (Fig. 10d). The other possible consequence of the MY28 dust storm activity is a shift to the north of the registered north polar hood edge about 5° with respect to MY27 observations.

Acknowledgments

This work was supported by the Belgian Scientific Policy office under grant MO/035-017. We thank our reviewers for careful and constructive comments.

References

Bell III, J.F., 1996. Iron, sulfate, carbonate, and hydrated minerals on Mars. In: Dyar, M.D., McCammon, C., Schaefer, M.W. (Eds.), Mineral Spectroscopy: A Tribute to Roger G. Burns, Spec. Publ. Geochem. Soc. Vol. 5, pp. 359–380.

Benson, J.L., James, P.B., 2005. Yearly comparisons of the martian polar caps: 1999–2003 mars orbiter camera observations. Icarus 174 (2), 513–523.

Benson, J.L., Bonev, B.P., James, P.B., Shan, K.J., Cantor, B.A., Caplinger, M.A., 2003. The seasonal behavior of water ice clouds in the Tharsis and Valles Marineris regions of Mars: Mars Orbiter camera. Icarus 165, 34–52.

Benson, J.L., James, P.B., Cantor, B.A., Remigio, R., 2006. Interannual variability of water ice clouds over major martian volcanoes observed by MOC. Icarus 184, 365–371.

Bertaux, J.L., Fonteyn, D., Korablev, O., Chassefiere, E., Dimarellis, E., Dubois, J.P., Hauchecorne, A., Cabane, M., Rannou, P., Levasseur-Regourd, A.C., Cernogora, G., Quemerais, E., Hermans, C., Kockarts, G., Lippens, C., De Maziere, M., Moreau, D., Muller, C., Neefs, B., Simon, P.C., Forget, F., Hourdin, F., Talagrand, O., Moroz, V.I., Rodin, A., Sandel, B., Stern, A., 2000. The study of the Martian atmosphere from top to bottom with SPICAM light on mars express. Planet. Space Sci. 48, 1303–1320.

Bertaux, J.-L., Korablev, O., Perrier, S., Quemerais, E., Montmessin, F., Leblanc, F., Lebonnois, S., Rannou, P., Lefevre, F., Forget, F., Fedorova, A., Dimarellis, E., Reberac, A., Fonteyn, D., Chaufray, J.Y., Guibert, S., 2006. SPICAM on mars express: Observing modes and overview of UV spectrometer data and scientific results. J. Geophys. Res. 111, E10S90.

Cantor, B.A., James, P.B., Caplinger, M., Wolff, M.J., 2001. Martian dust storms: 1999 mars orbiter camera observations. J. Geophys. Res. 106 (E10), 23653–23687.

Christensen, P.R., Bandfield, J.L., Hamilton, V.E., Ruff, S.W., Kieffer, H.H., Titus, T.N., Malin, M.C., Morris, R.V., Lane, M.D., Clark, R.L., Jakosky, B.M., Mellon, M.T., Pearl, J.C., Conrath, B.J., Smith, M.D., Clancy, R.T., Kuzmin, R.O., Roush, T., Mehall, G.L., Gorelick, N., Bender, K., Murray, K., Dason, S., Greene, E., Silverman, S., Greenfield, M., 2001. Mars global surveyor thermal emission spectrometer experiment: Investigation description and surface science results. J. Geophys. Res. 106 (E10), 23823–23871.

Clancy, R.T., Lee, S.W., 1991. A new look at dust and clouds in the mars atmosphere: Analysis of emission-phase-function sequences from global viking IRTM observations. Icarus 93, 135–158.

Clancy, R.T., Grossman, A.W., Wolff, M.J., James, P.B., Rudy, D.J., Billawala, Y.N., Sandor, B.J., Lee, S.W., Muhleman, D.O., 1996. Water vapor saturation at low latitudes around aphelion: A key to mars climate? Icarus 122, 36–62.

Clancy, R.T., Sandor, B.J., Wolff, M.J., Christensen, P.R., Smith, M.D., Pearl, J.C., Conrath, B.J., Wilson, R.J., 2000. An intercomparison of ground-based millimeter, MGS TES, and viking atmospheric temperature measurements: Seasonal and interannual variability of temperatures and dust loading in the global mars atmosphere. J. Geophys. Res. 105, 9553–9572.

Clancy, R.T., Wolff, M.J., Christensen, P.R., 2003. Mars aerosol studies with the MGS TES emission phase function observations: Optical depths, particle sizes, and ice cloud types versus latitude and solar longitude. J. Geophys. Res. 108 (E9), 5098.

Evans, K.F., 1998. The spherical harmonics discrete ordinate method for three-dimentional atmospheric radiative transfer. J. Atm. Sci. 55, 429–446.

Forget, F., Hourdin, F., Fournier, R., Hourdin, C., Talagrand, O., Collins, M., Lewis, S.R., Read, P.L., Huot, J.-P., 1999. Improved general circulation models of the Martian atmosphere from the surface to above 80 km. J. Geophys. Res. 104 (E10), 24155–24176.

Hapke, B., 1986. Bidirectional reflectance spectroscopy. 4. The extinction coefficient and the opposition effect. Icarus 67, 264–280.

Hinson, D.P., Wilson, R.J., 2004. Temperature inversions, thermal tides, and water ice clouds in the Martian tropics. J. Geophys. Res. 109 (E1).

James, P.B., Clancy, R.T., Lee, S.W., Martin, L.J., Singer, R.B., Smith, E., Kahn, R.A., Zurek, R.W., 1994. Monitoring mars with the Hubble space telescope: 1990–1991 observations. Icarus 109, 79–101.

Key, J.R., Yang, P., Baum, B.A., Nasiri, S.L., 2002. Parameterization of shortwave ice cloud optical properties for various particle habits. J. Geophys. Res. 107 (D13), 4181.

Lefevre, F., Bertaux, J.-L., Clancy, R.T., Encrenaz, T., Fast, K., Forget, F., Lebonnois, S., Montmessin, F., Perrier, S., 2008. Heterogeneous chemistry in the atmosphere of mars. Nature 454.

Lewis, S.R., Montabone, L., Read, P.L., Rogberg, P., 2006. Data assimilation for Mars: an overview of results from the mars global surveyor period, proposals for future plans and requirements for open access to assimilation output. Second workshop on Mars Atmosphere Modelling and Observations February 27–March 3, 2006, Granada, Spain.

Malin, M.C., Calvin, W.M., Cantor, B.A., Clancy, R.T., Haberle, R.M., James, P.B., Thomas, P.C., Wolff, M.J., Bell, J.F., Lee, S.W., 2008. Climate, weather, and north polar observations from the mars reconnaissance orbiter mars color imager. Icarus 194.

Mateshvili, N., Fussen, D., Vanhellemont, F., Bingen, C., Dodion, J., Montmessin, F., Perrier, S., Dimarellis, E., Bertaux, J.-L., 2007a. (Paper I) Martian ice cloud distribution obtained from SPICAM nadir UV measurements. J. Geophys. Res. 112, E07004.

Mateshvili, N., Fussen, D., Vanhellemont, F., Bingen, C., Dodion, J., Montmessin, F., Perrier, S., Bertaux, J.L., 2007b. Detection of Martian dust clouds by SPICAM UV nadir measurements during the October 2005 regional dust storm. Adv. Space Res. 40 (N6), 869–880.

Mateshvili, N., Fussen, D., Vanhellemont, F., Bingen, C., Dodion, J., Daerden, F.,Verhoeven, C., Montmessin, F., Bertaux, J.-L., 2007c. Ice and dust clouds in the Martian atmosphere: results from SPICAM UV channel nadir measurements. European Space Agency. European Mars Science and Exploration Conference: Mars Express & ExoMars ESTEC, Noordwijk, The Netherlands, 12–16 November, 〈http://www.rssd.esa.int/SYS/docs/ll_transfers/S06_1045_mateshvili.pdf〉.

McKim, R., 2006. Mars in 2005: first interim report. J. Br. Astron. Assoc. 116 (1), 6.

Pearl, J.C., Smith, M.D., Conrath, B.J., Bandeld, J.L., Christensen, P.R., 2001. Observations of Martian ice clouds by the mars global surveyor thermal emission spectrometer: the first Martian year. J. Geophys. Res. 106, 12325–12338.

Perrier, S., Bertaux, J.L., Lefevre, F., Lebonnois, S., Korablev, O., Fedorova, A., Montmessin, F., 2006. Global distribution of total ozone on mars from SPICAM/MEX UV measurements. J. Geophys. Res. 111, E09S06.

Smith, M.D., 2004. Annual variability in TES atmospheric observations of mars during 1999–2003. Icarus 167, 148–165.

Smith, D., Neumann, G., Arvidson, R. E., Guinness, E. A., Slavney, S., 2003a. Mars Global Surveyor Laser Altimeter Mission Experiment Gridded Data Record. NASA Planetary Data System, MGS-M-MOLA-5-MEGDR-L3-V1.0.

Smith, M.D., Bandfield, J.L., Christensen, P.R., Richardson, M.I., 2003b. Thermal emission imaging system (THEMIS) infrared observations of atmospheric dust and water ice cloud optical depth. J. Geophys. Res. 108 (E11), 5115.

Tamppari, L.K., Zurek, R.W., Paige, D.A., 2000. Viking era water-ice clouds. J. Geophys. Res. 105, 4087–4107.

Tamppari, L.K., Smith, M.D., Bass, D.S., Hale, A.S., 2008. Water-ice clouds and dust in the north polar region of mars using MGS TES data. Planetary and Space Science 56, 227–245.

Titus, T.N., 2005. Mars polar cap edges tracked over 3 full mars years. Lunar and Planetary Science XXXVI (2005), March 14–18, 2005, in League City, Texas, abstract no. 1993.

Wang, H., Ingersoll, A.P., 2002. Martian clouds observed by mars global surveyor mars orbiter camera. J. Geophys. Res. 107 (E10), 5078.

Warren, S.G., 1984. Optical properties of ice from the ultraviolet to the microwave. Appl. Opt. 23, 1206–1225.

Wolff, M.J., Clancy, R.T., 2003. Constraints on the size of Martian aerosols from thermal emission spectrometer observations. J. Geophys. Res. 108 (E9), 5097.

Wolff, M.J., Bell, J.F., James, P.B., Clancy, R.T., Lee, S.W., 1999. Hubble space telescope observations of the Martian aphelion cloud belt prior to the pathfinder. J. Geophys. Res. 104 (E4), 9027–9041.

Zasova, L., Formisano, V., Moroz, V., Grassi, D., Ignatiev, N., Giuranna, M., Hansen, G., Blecka, M., Ekonomov, A., Lellouch, E., Fonti, S., Grigoriev, A., Hirsch, H., Khatuntsev, I., Mattana, A., Maturilli, A., Moshkin, B., Patsaev, D., Piccioni, G., Rataj, M., Saggin, B., 2005. Water clouds and dust aerosols observations with PFS MEX at mars. Planetary and Space Science 53, 1065–1077.